Materials Science & Engineering A 760 (2019) 359–365

Contents lists available at ScienceDirect

Materials Science & Engineering A

journal homepage: www.elsevier.com/locate/msea

Tuning the mechanical behavior of high-entropy alloys via controlling cooling rates

Jia Li[a], Haotian Chen[a], Sixu Li[a], Qihong Fang[a,*], Yong Liu[b], Luxing Liang[b], Hong Wu[b,**], Peter K. Liaw[c,***]

[a] State Key Laboratory of Advanced Design and Manufacturing for Vehicle Body, Hunan University, Changsha, 410082, PR China
[b] State Key Laboratory of Powder Metallurgy, Central South University, Changsha, 410083, PR China
[c] Department of Materials Science and Engineering, The University of Tennessee, Knoxville, TN, 37996, USA

ARTICLE INFO

Keywords:
Cooling rate
Molecular dynamics simulation
Solidification
High-entropy alloys
Plastic deformation

ABSTRACT

The microstructures determine the macro-mechanical properties in metals and alloys. However, the formation mechanism of microstructures in high-entropy alloys (HEAs) rapidly cooled to room temperature still remains unknown at nanoscale. Here, we present the AlCoCrCuFeNi HEAs prepared by various cooling rates and the deformation behaviour using molecular dynamic simulation. The results show that the radial distribution function of HEAs is in good agreement with the previous experimental result. The amorphous HEA is formed at high cooling rates, while the nanocrystalline HEA is generated at low cooling rates. The hybrid amorphous-crystallization structured HEA occurs at middle cooling rates. For low cooling rates, the considerable amount of face-centered-cubic and hexagonal-close-packed short-range orders clearly show the crystal-nucleation process in the supercooled liquid of HEAs. The high residual hydrostatic stress around grain boundaries is observed in the nanocrystaline HEAs. Moreover, the nanocrystal HEA presents a high strength, compared to the amorphous HEA. The amorphous HEA exhibits the stable flow stress due to no obvious local stress concentration. This result could help guide the preparation of HEAs with a high strength by controlling the cooling rate, which generates the structural hierarchy.

1. Introduction

Multi-component high entropy alloys (HEAs) with at least five equal or near-equal atomic-ratio principle elements have drawn great attention during the past decades [1–5], due to high hardness, great wear and oxidation resistance, corrosion, fatigue and fracture resistance, and high thermostability [6–12]. These properties give HEAs the potential to be applied in applications such as mechanical parts in factories producing corrosive products, molds, function films and even naval applications [13–17].

Recently, the AlCoCrCuFeNi HEAs have been well investigated owing to their great mechanical properties, such as a favorable thermostability [18], and considerable hardness up to 420Hv [19]. Based on the previous work, the phase decomposition [20,21], element effect [18,22,23] and phase transformation [24] in AlCoCrCuFeNi HEAs have been studied. As well known, the solidification of pure metal plays a key role in affecting mechanical properties [25–28]. The solidification of metallic materials involves the thermal processes, in which the grain growth is a key phenomenon to determine the size and morphology of the microstructure. Therefore, it is essential to control the grain-growth process to obtain designed products [29–33].

The influence of cooling rate on phase formation in HEAs has been reported [34–38]. For example, the presence of precipitates relies on the low cooling rate approaching 1K/s, but Cu-rich precipitates do not form in the as cast material [34,35]. The relationship between the critical cooling rates and the parameters (atomic size difference, mixing enthalpy, mixing entropy, and electronegativity) is simply established, to predict phases (amorphous phase, solid solution phase, or intermetallic phase) and design high-entropy bulk metallic glasses (HE-BMGs) [36,37]. Regardless of cooling rate, the dominant phase changes from a face-centered cubic (FCC) to body-centered cubic (BCC) structures with the variation of the mixing entropy in the $Al_xCoCrCuFeNi$ HEAs [38]. However, it is not straightforward to observe the experimentally homogeneous nucleation of metals and alloys cooled from

* Corresponding author.
** Corresponding author.
*** Corresponding author.
E-mail addresses: fangqh1327@hnu.edu.cn (Q. Fang), hwucsu@csu.edu.cn (H. Wu), pliaw@utk.edu (P.K. Liaw).

https://doi.org/10.1016/j.msea.2019.06.017
Received 20 April 2019; Received in revised form 4 June 2019; Accepted 5 June 2019
Available online 06 June 2019
0921-5093/

high temperatures. Each stage of the solidification process can be revealed by various computational approaches, including Monte Carlo simulation, cellular automaton simulation, and phase-field simulation [25–28]. Since these methods are based on phenomenological models, it is generally impossible to study nucleation inherently in accordance with various rules to obtain a reasonable microstructure. To solve these critical issues, molecular dynamics (MD) simulations have been widely employed to reveal the nature of nucleation at the atomistic scale [29–33]. For example, the formation of solidification defects and tensile-deformation-driven evolution in the solidified polycrystalline aluminum at different quench rates are investigated by MD simulations in detail [29]. The homogeneous nucleation from an undercooled iron melt occurs using a billion-atom MD simulation, revealing that some satellite-like small grains surrounding previously formed large grains exist in the middle of the nucleation process [31–33]. Hence, based on the results above mentioned, the relationship between the structure and solidification at a nanoscale still remains unknown in AlxCoCrCuFeNi HEAs cooled at different cooling rates.

Motivated by above-mentioned challenges, using MD simulations, we explore the solidification process of HEAs at different cooling rates. Our focus is on the microstructure-formation mechanism at the atomic scale under the tension loading. In this way, the physical interpretations of the nanocrystalline and amorphous HEA are also expected. This paper is organized as follows: A detailed description of the MD simulation details is given in Section 2. Moreover, the simulation parameters of tension tests are presented by MD simulations. In Section 3, the results of the solidification and deformation in the HEA are modeled with the MD simulation. The radial distribution function (RDF), grain size, grain number, and mechanical properties in HEAs are presented in Section 3. Based on the current results obtained with MD simulations, the relationship between the cooling rate and mechanical property is studied in these HEAs. Some discussions on the deformation behaviour and cooling rate is studied in Section 4. Finally, the mainly results are summarized and concluded in Section 5.

2. MD simulation details

The AlCoCrCuFeNi HEA is built in Fig. 1, where atoms are colored according to their atom types. This size of the free-standing HEA film sample containing 3.6 million atoms is $107.9 \times 3.6 \times 107.9\,\mathrm{nm}^3$. The AlCoCrCuFeNi HEA is obtained, based on the heating process, as follows: (a) atoms of the AlCoCrCuFeNi HEA are randomly positioned at the FCC crystal structure sites with the temperature of 300 K; (b) in the heating stage, all atoms are heated to 3300 K at the heating rate of 1×10^{14} K/s and their velocities are relaxed until an equilibrium condition is obtained at the temperature of 3300 K; (c) in the quenching stage, quick cooling is simulated by reducing the environmental temperature to 300 K with quenching at different cooling rates, and relaxing to a position of equilibrium at the temperature of 300 K [39]. The AlCoCrCuFeNi HEA is applied with the constant strain rate of $1 \times 10^9\,\mathrm{s}^{-1}$ along the x direction under the isothermal–isobaric (NPT) ensemble with a zero-pressure condition [39,40]. Periodic boundary conditions are maintained along all directions in the MD model [41–43]. Here, the preparation and tension of HEA sample are created by a large-scale atomic/molecular massively parallel simulator (LAMMPS) package software [44], and the OVITO software is employed to for the analysis of defects [45]. The common neighbour analysis (CNA) is used to determine the defects during the cooling and deformation processes. Here, based on CNA, the FCC atoms, BCC atoms, HCP atoms, and non-structured atoms (such as, amorphous structures or grain boundaries or dislocation cores) are green, blue, pink, and white, respectively. Hence, the BCC structured nanocrystalline HEA is defined as the grain size less than 100 nm, the amorphous HEA is defined as the disordered structure, and the hybrid structured HEA includes amorphous phase and nanocrystal phase.

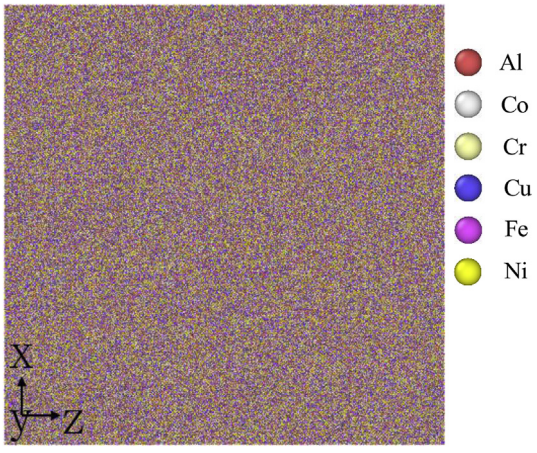

Fig. 1. The atomic model of the AlCoCrCuFeNi HEA.

For the atom interactions in the AlCoCrCuFeNi HEA, we have used the embedded atom method (EAM) potential, which is a multi-body potential energy function in the following form [46,47].

$$E = F_\alpha \sum_{j \neq i} \rho_i(R_{i,j}) + \frac{1}{2} \sum_{j \neq i} \varphi_{\alpha,\beta}(R_{i,j}) \tag{1}$$

where the total energy, E, on atom, i, is the sum of the embedding energy F, and the short-range pair potential energy φ. ρ is the electron density. α and β are the elemental types of atoms i and j, respectively. This EAM is developed based on the previous work [46–48], which is used to study the tensile properties, and thin film growth and annealing [49–52].

The average viral stress can be obtained, as followed [43].

$$S = \frac{1}{\Omega} \sum_{i}^{N} \left(m_i v_i \otimes \ v_i + \frac{1}{2} \sum_{i \neq j} r_{ij} \otimes \ \frac{\partial U(r_{ij})}{\partial r_{ij}} \right) \tag{2}$$

where S presents the average viral stress with six components, Ω means the volume of the cut-off domain, m_i is the mass, v_i is the velocity of the atom i, $\otimes$ is the tensor product of two vectors, and N is the total number atoms in the domain.

3. Results and discussion

Fig. 2 shows the evolution of the temperature, structure and volume during the process of melting and solidification. As the temperature increases, the amorphous phase nucleates from the FCC HEA matrix. When the temperature continues to rise to 3300 K higher than the melting point, the solid phase changes into the liquid phase (see the microstructure in Fig. 2b). The liquid phase at high temperatures is cooled to room temperature at the cooling rate of 1×10^{14} K/s, and then the amorphous HEA is prepared. The volume in the HEA matrix experiences a rapid increase, and then a steady linear increase during the melting stage (Fig. 2c). However, the volume decreases monotonously linearly during the solidification, owing to the formation of the amorphous structure. This result about the amorphous HEA is proved in Fig. 2b.

The cooling rate plays a key role in affecting the microstructure phase during solidification. Based on the previous work, the cooling rate is divided into the conventional die casting (10^1–10^3 K/s), melt spinning (10^5–10^6 K/s) [53], liquid splat-quenching (10^9–10^{10} K/s) [54], and pulsed laser quenching (10^{12}–10^{13} K/s) [55,56]. Here, the fast cooling rate in the range from 1×10^{12} K/s to 1×10^{14} K/s [55,56] is considered, due to the limit of the computation ability [56–59]. At the temperature of 800 K, many small grains appear and grow larger with the decreasing temperature (see Fig. 3). Furthermore, the new nucleation also occurs in the remaining part of the undercooled melt for various cooling rates. When the temperature is 300 K, the only BCC

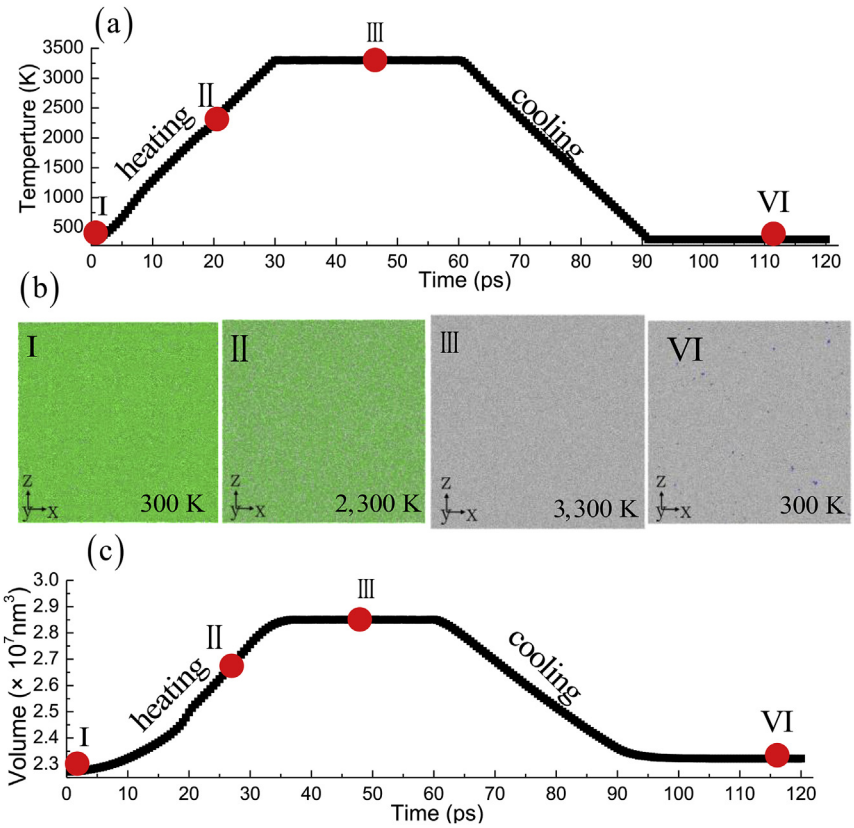

Fig. 2. Temperature vs. time at three stages: heating to 3300 K at the heating rate of 1×10^{14} K/s, keeping the temperature of 3300 K, and cooling to 300 K at the cooling rate of 1×10^{14} K/s in the AlCoCrCuFeNi HEA (a). The corresponding atomic structure as shown in (b), where atoms are colored according to CNA. In addition, "*I*" stands for initial FCC structure, "*II*" stands for the structure at high temperature of 2300 K, "*III*" stands for the liquid or melted state, and "*VI*" stands for amorphous structure. Volume vs. time at three stages in (c).

phase occurs for the cooling rate lower than 5×10^{12} K/s, the stable BCC phase and amorphous phase can coexist at cooling rates from 1×10^{13} K/s to 2.5×10^{13} K/s, and the only amorphous phase takes place at cooling rates higher than 5×10^{13} K/s. Some annealing twins (see Fig. 4) generate at cooling rates lower than 1×10^{13} K/s, complying with the experimental results [60–62].

Fig. 5 presents the distribution of the residual hydrostatic stress, which is equal to $(\sigma_x + \sigma_y + \sigma_z)/3$. The red atoms mean the high tensile stress, and the blue atoms stand for the high compressive stress. It is noticed that the HEA samples cooled shows the high residual hydrostatic stress around the grain boundaries (Fig. 5a–c). Compared to the BCC HEA and the hybrid-structured HEA, the amorphous HEA presents a more complex distribution of stresses (Fig. 5d–f), which would affect its mechanical property and deformation mechanism. The current results agree with the previous work, which indicates the high levels of residual stresses generated when the metals and alloys are cooling down from the fabrication temperature to room temperature [63,64]. Here, the role of the cooling rate on the levels of residual stresses at room temperature can be revealed in HEAs (Fig. 5).

The total number of grains and the radial distribution function (RDF) at different cooling rates are shown in Fig. 6a and b, respectively. RDF can be used to analyze the structural changes [65]. Here, the number of grains is counted when the grain size is larger than 0.5 nm. In Fig. 6a, the grain size declines continuously with increasing the cooling rate. The grain number firstly increases, and then decreases with increasing the cooling rate. The turning point of this change occurs at the cooling rate of 5×10^{12} K/s, in good agreement with the RDF curve (Fig. 6b). When the cooling rate is larger than 5×10^{12} K/s, the RDF curve has a significant change in the peak, indicating that the nucleation of an amorphous structure occurs. Fig. 6c displays the stress-strain curve in HEAs prepared by different cooling rates, and the corresponding RDF of the HEA sample is exhibited in Fig. 6d. For the nanocrystalline HEA, the yielding strength is higher than the hybrid-structured and amorphous HEAs. However, the amorphous HEA presents the non-obvious softening effect, compared to the hybrid-structured HEA and amorphous HEAs.

The formation of microstructures, including the grain boundary, twinning boundary, and dislocation, is presented in Fig. 7. The

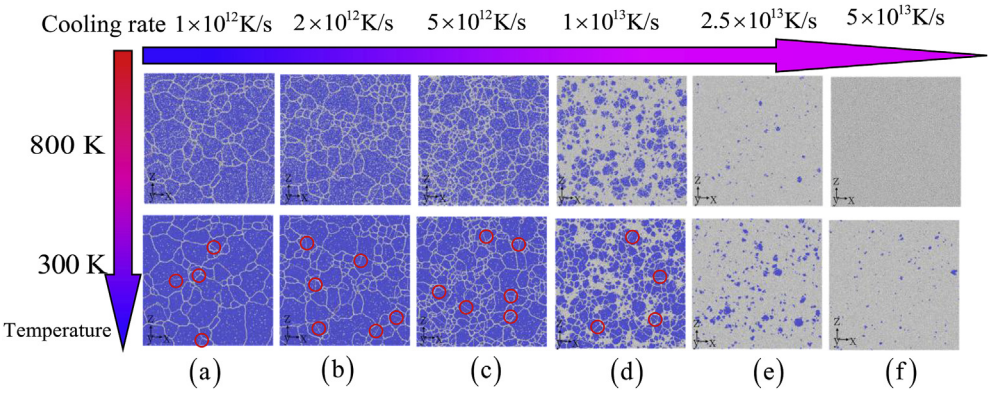

Fig. 3. The microstructural evolution of the cooled HEA at different temperatures and cooling rates: 1×10^{12} K/s (a), 2×10^{12} K/s (b), 5×10^{12} K/s (c), 1×10^{13} K/s (d), 2.5×10^{13} K/s (e), and 5×10^{13} K/s (f). The red circles represent the annealing twins at the temperature of 300 K. The atoms are colored according to CNA. (For interpretation of the references to color in this figure legend, the reader is referred to the Web version of this article.)

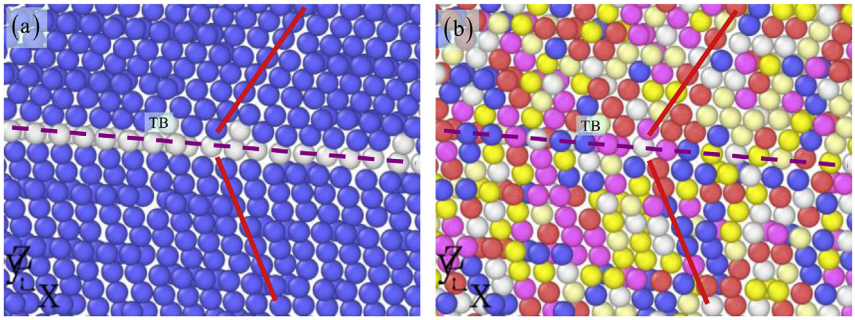

Fig. 4. The annealing twins at the temperature of 300 K and cooling rate of 2×10^{12} K/s. TB represents the annealing twin boundary.

deformation twinning occurs at cooling rates of 1×10^{12} K/s and 2×10^{12} K/s. The formation of twinning is a key plastic-deformation mechanism in BCC metals and alloys [7,10,40,67]. Hence, the BCC nanocrystalline HEAs subjected to the tensile loading produce the deformation twinning, to coordinate the plastic deformation. Recent experiments suggest that the deformation twinning not only control deformation, but also affect the mechanical properties in HEAs [66,67]. The abnormal grain growth is also observed in the nanocrystalline HEA, which is in good agreement with the previous experimental results related to the grain growth in Ni-based alloys during the deformation process [68]. These special phenomena have important effects on mechanical properties, which has been proved in previous experiments [66–68]. The nucleation of small grains takes place in the hybrid-structured HEA. However, the microstructure basically has not changed in the amorphous HEA, due to the no obvious stress concentration.

To reveal the relationship between the stress distribution and mechanical properties, Fig. 8 exhibits the stress distribution of the HEA by atomic simulations. The red atom means the high tensile stress, and the blue atom represents the high compressive stress. As a result, the high stress concentration is produced at the grain boundary due to the elastic mismatch or inhomogeneous flow in each grain, especially in the nanocrystalline HEA [69]. For the hybrid-structured HEA and the amorphous HEA, there are no obvious local stress concentration. The more point-concentrated stresses are distributed in the HEA with the amorphous region, which leads to the stable flow stress (Fig. 6c).

According to the previous report [70,71], the predominant plastic deformation mechanisms of amorphous metals and their composites are the formation of shear bands (SBs), which occur by means of the relative sliding of two or several parts of the material. To reveal the effect of the cooling rate on the morphology of the SBs, Fig. 9 demonstrates the shear strain configurations of HEAs at the strain of 10%. As a result, the morphology of the SBs can be effectively controlled by tuning the cooling rate, due to the difference of micostructure (Fig. 7). For the amorphous HEAs, some parallel mature SBs are generated by the stochastic nucleation, coalescence and growth of shear transformation zones in Fig. 9(e–g) [72]. Due to the existence of elemental heterogeneous distribution in the disordered structure, the SBs hardly penetrate the whole sample when the formation of embryonic SBs, which is different from the conventional behavior of metal glass [70–72]. However, for the nanocrystalline HEA, the plastic deformation is mainly concentrated in the two main SBs (Fig. 9a–c). As shown in Fig. 9d, a high density of local networks of tiny SBs and dislocations are observed in the hybrid structured HEA. Hence, the deformation modes could transit from pronounced individual shear banding to homogeneous-like co-deformation, which can be achieved by introducing the crystalline HEA. As a result, the yielding strength and reduced stress continuously declines with the decreasing cooling rate, regardless of the microstructural evolutions (Fig. 10). The softening parameter, δ, is $(\sigma_y - \sigma_c)/\sigma_y$, where σ_y is yielding strength, and σ_c is the minimum stress after yielding and before fracture. Moreover, the amorphous phase can reduce the effect of softening by the shear banding deformation, and the existence of amorphous phase could improve the structural stability (softening parameter in Fig. 10).

4. Conclusions

The microstructures and mechanical properties of the rapidly-quenched HEA at various cooling rates are studied by MD simulations. The calculated RDF in a solid state agrees well with the experimental data. The high cooling rates produce the glass formation, while low

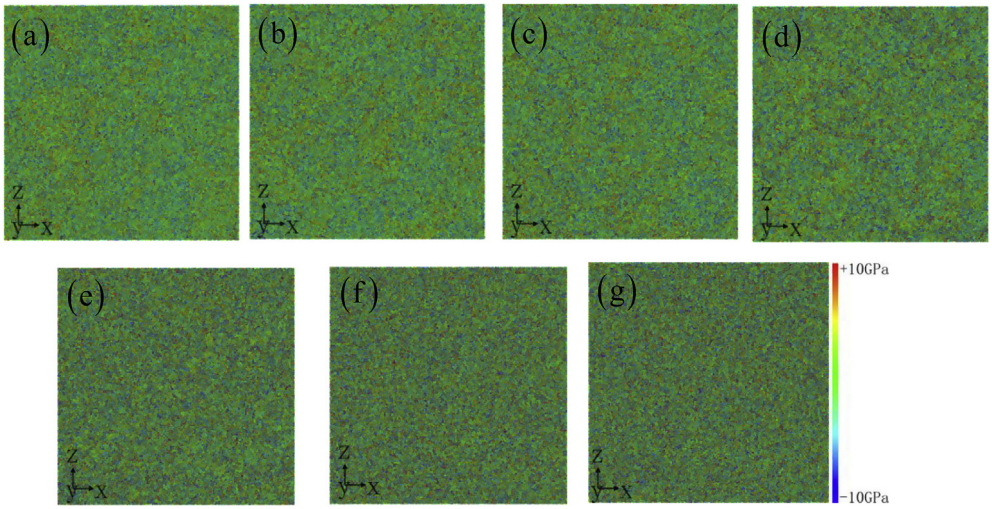

Fig. 5. The residual hydrostatic stress distribution of the microstructure at room temperature and the cooling rates: 1×10^{12} K/s (a), 2×10^{12} K/s (b), 5×10^{12} K/s (c), 1×10^{13} K/s (d), 2.5×10^{13} K/s (e), 5×10^{13} K/s (f), and 1×10^{14} K/s (g).

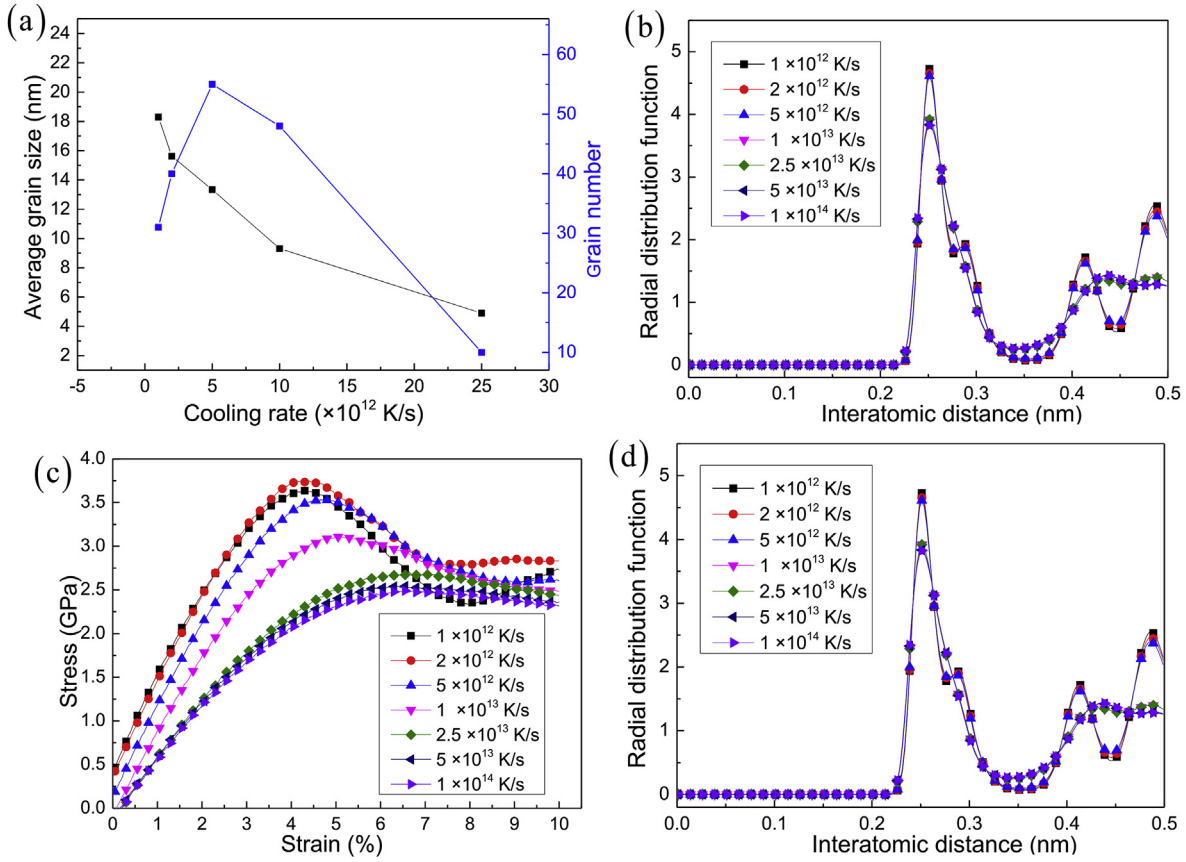

Fig. 6. The relationship between the grain size (grain number) and cooling rate (a). RDF vs. cooling rate after the cooling process (b). The relationship of the stress and strain at the different cooling rates (c). RDF vs. cooling rate after the tension (d).

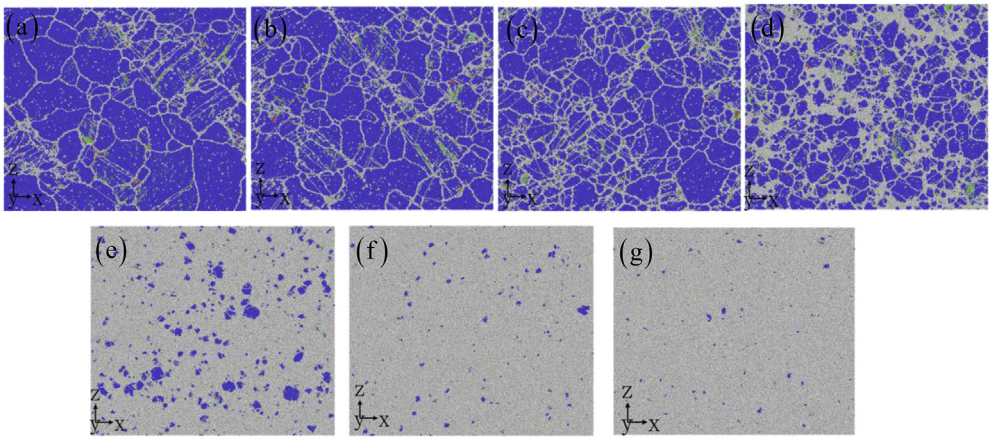

Fig. 7. The microstructure evolution at the strain of 10% and the cooling rates: 1×10^{12} K/s (a), 2×10^{12} K/s (b), 5×10^{12} K/s (c), 1×10^{13} K/s (d), 2.5×10^{13} K/s (e), 5×10^{13} K/s (f), and 1×10^{14} K/s (g). According to CNA, the atoms are colored.

cooling rates result in crystallization. The beginning stage of solidification desponds on the cooling rate, which controls the size and location of nucleation. Furthermore, the nucleation process from the supercooled HEA is presented in a wide range of cooling rates from 1×10^{12} K/s to 1×10^{14} K/s, and the grain size and number are estimated for different cooling rates. The low cooling rate leads to a high strength, but brings about serious softening in HEAs. The high cooling rate causes the low strength, but yields the stable stress flow.

Data availability

The datasets generated and/or analyzed during the current study are available from the corresponding author on reasonable request.

Acknowledgements

The authors would like to deeply appreciate the support from the Foundation for Innovative Research Groups of the National Natural Science Foundation of China (Grant No. 51621004), the National Natural Science Foundation of China (51871092, 11772122, 51771233, 51625404, 51601224, 51771232, and 51671217), State Key Laboratory of Advanced Design and Manufacturing for Vehicle Body (71865015), the Fundamental Research Funds for the Central Universities (531107051151), Key Research and Development Program of Hunan

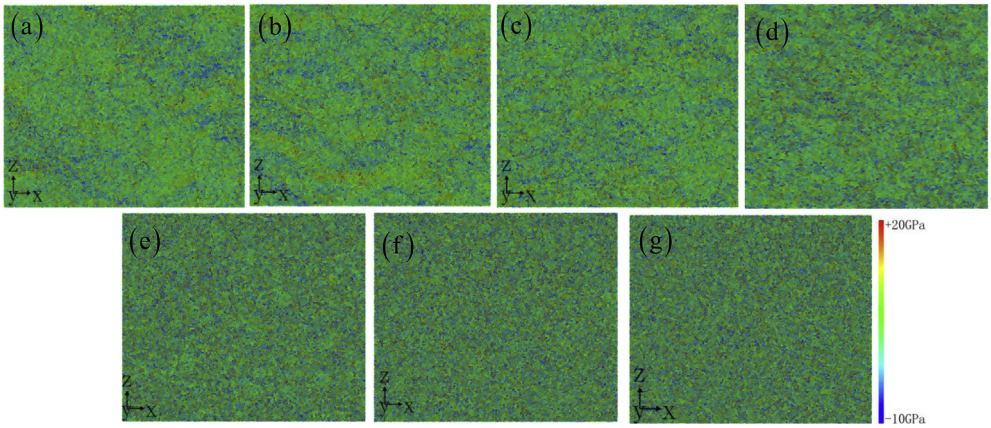

Fig. 8. The stress distribution of microstructure at the strain of 10% and the cooling rates: 1×10^{12} K/s (a), 2×10^{12} K/s (b), 5×10^{12} K/s (c), 1×10^{13} K/s (d), 2.5×10^{13} K/s (e), 5×10^{13} K/s (f), and 1×10^{14} K/s (g).

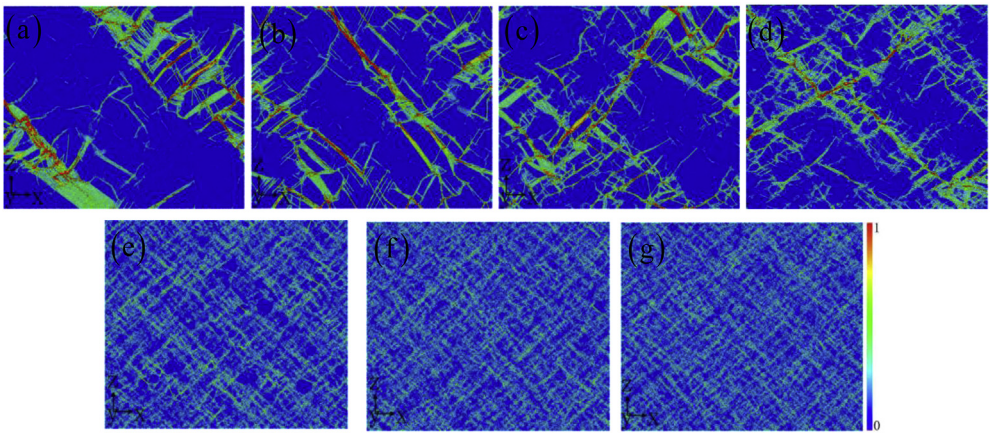

Fig. 9. The shear strain distribution of microstructure at the strain of 10% and the cooling rates: 1×10^{12} K/s (a), 2×10^{12} K/s (b), 5×10^{12} K/s (c), 1×10^{13} K/s (d), 2.5×10^{13} K/s (e), 5×10^{13} K/s (f), and 1×10^{14} K/s (g).

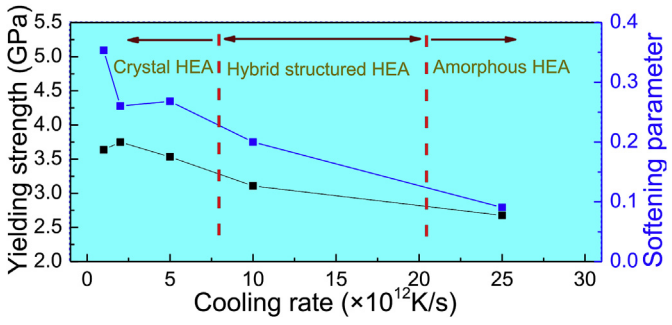

Fig. 10. The relationship between mechanical properties and cooling rate.

Province (Grant No. 2016JC2003), China Postdoctoral Science Foundation (Grant No. 2018M633164), Central South University Postgraduate Independently Explore Innovative Program (Grant No. 2018ZZTS127), and the National Key Research and Development Program of China (2016YFB0700300 and 2016YFB1100103). PKL would like to acknowledge the Department of Energy (DOE), Office of Fossil energy, National Energy Technology Laboratory (DE-FE-0011194) with the program manager, Dr. J. Mullen. PKL very much appreciates the support of the U.S. Army Research Office project (W911NF-13-1-0438 and W911NF-19-2-0049) with the program managers, Drs. M.P. Bakas, S.N. Mathaudhu, and D.M. Stepp. PKL thanks the support the National Science Foundation (DMR-1611180 and 1809640) with the program directors, Drs. G. Shiflet and D. Farkas.

References

[1] J.W. Yeh, S.K. Chen, S.J. Lin, J.Y. Gan, T.S. Chin, T.T. Shun, C.H. Tsau, S.Y. Chang, Nanostructured high-entropy alloys with multiple principal elements: novel alloy design concepts and outcomes, Adv. Eng. Mater. 6 (2004) 299–303.
[2] H.Y. Diao, R. Feng, K.A. Dahmen, P.K. Liaw, Fundamental deformation behavior in high-entropy alloys: an overview, Curr. Opin. Solid State Mater. Sci. 21 (2017) 252–266.
[3] Y. Zhang, T.T. Zuo, Z. Tang, M.C. Gao, K.A. Dahmen, P.K. Liaw, Z.P. Lu, Microstructures and properties of high-entropy alloys, Prog. Mater. Sci. 61 (2014) 1.
[4] M.C. Gao, J.W. Yeh, P.K. Liaw, Y. Zhang, High-Entropy Alloys, Springer International Publishing, 2016.
[5] S.S. Nene, M. Frank, K. Liu, S. Sinha, R.S. Mishra, B.A. McWilliams, K.C. Cho, Corrosion-resistant high entropy alloy with high strength and ductility, Scripta Mater. 166 (2019) 168–172.
[6] M.A. Hemphill, T. Yuan, G.Y. Wang, J.W. Yeh, C.W. Tsai, A. Chuang, P.K. Liaw, Fatigue behavior of Al0.5CoCrCuFeNi high entropy alloys, Acta Mater. 60 (2012) 5723–5734.
[7] Z. Tang, T. Yuan, C.W. Tsai, J.W. Yeh, C.D. Lundin, P.K. Liaw, Fatigue behavior of a wrought Al0.5CoCrCuFeNi two-phase high-entropy alloy, Acta Mater. 99 (2015) 247–258.
[8] B. Gludovatz, A. Hohenwarter, K.V.S. Thurston, H. Bei, Z. Wu, E.P. George, R.O. Ritchie, Exceptional damage-tolerance of a medium-entropy alloy CrCoNi at cryogenic temperatures, Nat. Commun. 7 (2016) 10602.
[9] O.N. Senkov, J.M. Scott, S.V. Senkova, F. Meisenkothen, D.B. Miracle, C.F. Woodward, Microstructure and elevated temperature properties of a refractory TaNbHfZrTi alloy, J. Mater. Sci. 47 (2012) 4062–4074.
[10] Y. Shi, B. Yang, X. Xie, J. Brechtl, K.A. Dahmen, P.K. Liaw, Corrosion of AlxCoCrFeNi high-entropy alloys: Al-content and potential scan-rate dependent pitting behavior, Corros. Sci. 119 (2017) 33–45.
[11] Y. Shi, B. Yang, P.K. Liaw, Corrosion-resistant high-entropy alloys, A review, metals (basel) 7 (2017) 43.
[12] M. Seifi, D. Li, Z. Yong, P.K. Liaw, J.J. Lewandowski, Fracture toughness and fatigue crack growth behavior of as-cast high-entropy alloys, JOM 67 (2015) 2288–2295.

[13] K.V.S. Thurston, B. Gludovatz, A. Hohenwarter, G. Laplanche, E.P. George, R.O. Ritchie, Effect of temperature on the fatigue-crack growth behavior of the high-entropy alloy CrMnFeCoNi, Intermetallics 88 (2017) 65–72.
[14] K. Liu, M. Komarasamy, B. Gwalani, S. Shukla, R.S. Mishra, Fatigue behavior of ultrafine grained triplex Al0.3CoCrFeNi high entropy alloy, Scripta Mater. 158 (2019) 116–120.
[15] P.Y. Chen, C. Lee, S.Y. Wang, M. Seifi, J.J. Lewandowski, K.A. Dahmen, H.L. Jia, X. Xie, B.L. Chen, J.W. Yeh, C.W. Tsai, T. Yuan, P.K. Liaw, Fatigue behavior of high-entropy alloys: a review, Sci. China Technol. Sci. 61 (2018) 168–178.
[16] W. Li, G. Wang, S. Wu, P.K. Liaw, Creep, fatigue, and fracture behavior of high-entropy alloys, J. Mater. Res. 33 (2018) 3011–3034.
[17] D.B. Miracle, O.N. Senkov, A critical review of high entropy alloys and related concepts, Acta Mater. 122 (2017) 448–511.
[18] C.J. Tong, Y.L. Chen, J.W. Yeh, S.J. Lin, S.K. Chen, T.T. Shun, S.Y. Chang, Microstructure characterization of AlxCoCrCuFeNi high-entropy alloy system with multiprincipal elements, Metall. Mater. Trans. A 36 (2005) 881–893.
[19] C.C. Tung, J.W. Yeh, T.T. Shun, S.K. Chen, Y.S. Huang, H.C. Chen, On the elemental effect of AlCoCrCuFeNi high-entropy alloy system, Mater. Lett. 61 (2007) 1–5.
[20] S. Singh, N. Wanderka, B.S. Murty, U. Glatzel, J. Banhart, Decomposition in multi-component AlCoCrCuFeNi high-entropy alloy, Acta Mater. 59 (2011) 182–190.
[21] Y. Sun, P. Chen, L. Liu, M. Yan, X. Wu, C. Yu, Z. Liu, Local mechanical properties of AlxCoCrCuFeNi high entropy alloy characterized using nanoindentation, Intermetallics 93 (2018) 85–88.
[22] G. Qin, W. Xue, C. Fan, R. Chen, L. Wang, Y. Su, J. Guo, Effect of Co content on phase formation and mechanical properties of $(AlCoCrFeNi)_{100-x}Co_x$ high-entropy alloys, Mater. Sci. Eng. A 710 (2018) 200–205.
[23] A. Mao, P. Ding, F. Quan, T. Zhang, X. Ran, Y. Li, X. Gu, Effect of aluminum element on microstructure evolution and properties of multicomponent Al-Co-Cr-Cu-Fe-Ni nanoparticles, J. Alloy. Comp. 735 (2018) 1167–1175.
[24] Y.J. Zhou, Y. Zhang, F.J. Wang, G.L. Chen, Phase transformation induced by lattice distortion in multiprincipal component $CoCrFeNiCu_xAl_{1-x}$ solid-solution alloys, Appl. Phys. Lett. 92 (2008) 241917.
[25] G.S. Grest, D.J. Srolovitz, M.P. Anderson, Computer simulation of grain growth – IV. anisotropic grain boundary energy, Acta Metall. 33 (1985) 509–520.
[26] C.A. Gandin, M. A Rappaz, Coupled finite element-cellular automaton model for the prediction of dendritic grain structures in solidification processes, Acta Metall. Mater. 42 (1994) 2233–2246.
[27] L.Q. Chen, Phase-field models for microstructure evolution, Annu. Rev. Mater. Res. 32 (2002) 113–140.
[28] E. Miyoshi, T. Takaki, Extended higher-order multi-phase-field model for three-dimensional anisotropic-grain-growth simulations, Comput. Mater. Sci. 120 (2016) 77–83.
[29] B. Shen, C.Y. Liu, Y. Jia, G.Q. Yue, F.S. Ke, H.B. Zhao, K.M. Ho, Molecular dynamics simulation studies of structural and dynamical properties of rapidly quenched Al, J. Non-Cryst. Solids 383 (2014) 13–20.
[30] A. Mahata, M.A. Zaeem, Evolution of solidification defects in deformation of nano-polycrystalline aluminum, Comput. Mater. Sci. 163 (2019) 176–185.
[31] Y. Shibuta, S. Sakane, E. Miyoshi, S. Okita, T. Takaki, M. Ohno, Heterogeneity in homogeneous nucleation from billion-atom molecular dynamics simulation of solidification of pure metal, Nat. Commun. 8 (2017) 10.
[32] S. Okita, W. Verestek, S. Sakane, T. Takaki, M. Ohno, Y. Shibuta, Molecular dynamics simulations investigating consecutive nucleation, solidification and grain growth in a twelve-million-atom Fe-system, J. Cryst. Growth 474 (2017) 140–145.
[33] S. Okita, E. Miyoshi, S. Sakane, T. Takaki, M. Ohno, Y. Shibuta, Grain growth kinetics in submicrometer-scale molecular dynamics simulation, Acta Mater. 153 (2018) 108–116.
[34] E.J. Pickering, H.J. Stone, N.G. Jones, Fine-scale precipitation in the high-entropy alloy Al0.5CrFeCoNiCu, Mater. Sci. Eng. A 645 (2015) 65–71.
[35] N.G. Jones, K.A. Christofidou, H.J. Stone, Rapid precipitation in an Al0.5CrFeCoNiCu high entropy alloy, Mater. Sci. Technol. 31 (2015) 1171–1177.
[36] G.U.O. Sheng, C.T. Liu, Phase stability in high entropy alloys: formation of solid-solution phase or amorphous phase, Prog. Nat. Sci. Mater. Inter. 21 (2011) 433–446.
[37] Y. Zhang, Z.P. Lu, S.G. Ma, P.K. Liaw, Z. Tang, Y.Q. Cheng, M.C. Gao, Guidelines in predicting phase formation of high-entropy alloys, MRS Commun 4 (2014) 57–62.
[38] X.D. Xu, S. Guo, T.G. Nieh, C.T. Liu, A. Hirata, M.W. Chen, Effects of mixing enthalpy and cooling rate on phase formation of AlxCoCrCuFeNi high-entropy alloys, Materials 6 (2019) 100292.
[39] J. Li, Q.H. Fang, B. Liu, Y.W. Liu, Y. Liu, Mechanical behaviors of AlCrFeCuNi high-entropy alloys under uniaxial tension via molecular dynamics simulation, RSC Adv. 6 (2016) 76409–76419.
[40] L. Li, Q.H. Fang, J. Li, H. Wu, Origin of strengthening-softening trade-off in gradient nanostructured body-centred cubic alloys, J. Alloy. Comp. 775 (2019) 270–280.
[41] C. Huang, X. Peng, B. Yang, S. Weng, Y. Zhao, T. Fu, Grain size dependence of tensile properties in nanocrystalline diamond, Comput. Mater. Sci. 157 (2019) 67–74.
[42] Y. Cui, Y. Shibutani, S. Li, P. Huang, F. Wang, Plastic deformation behaviors of amorphous-Cu50Zr50/crystalline-Cu nanolaminated structures by molecular dynamics simulations, J. Alloy. Comp. 693 (2017) 285–290.
[43] J. Li, B. Liu, Q. Fang, Z. Huang, Y. Liu, Atomic-scale strengthening mechanism of dislocation-obstacle interaction in silicon carbide particle-reinforced copper matrix nanocomposites, Ceram. Int. 43 (2017) 3839–3846.
[44] S.J. Plimpton, A.P. Thompson, Computational aspects of many-body potentials, MRS Bull. 37 (2012) 513–521.
[45] A. Stukowski, Visualization and analysis of atomistic simulation data with OVITO–the Open Visualization Tool, Model. Simul. Mater. Sci. Eng. 18 (2009) 015012.
[46] M.S. Daw, S.M. Foiles, M.I. Baskes, The embedded-atom method: a review of theory and applications, Mater. Sci. Rep. 9 (1993) 251–310.
[47] X. Zhou, R. Johnson, H. Wadley, Misfit-energy-increasing dislocations in vapor-deposited CoFe/NiFe multilayers, Phys. Rev. B 69 (2004) 144113.
[48] Z. Lin, R.A. Johnson, L.V. Zhigilei, Computational study of the generation of crystal defects in a bcc metal target irradiated by short laser pulses, Phys. Rev. B 77 (2008) 214108.
[49] L. Xie, P. Brault, A.L. Thomann, X. Yang, Y. Zhang, G. Shang, Molecular dynamics simulation of Al–Co–Cr–Cu–Fe–Ni high entropy alloy thin film growth, Intermetallics 68 (2016) 78–86.
[50] Y. Afkham, M. Bahramyan, R.T. Mousavian, D. Brabazon, Tensile properties of AlCrCoFeCuNi glassy alloys: a molecular dynamics simulation study, Mater. Sci. Eng. A 698 (2017) 143–151.
[51] L. Xie, P. Brault, A.L. Thomann, J.M. Bauchire, AlCoCrCuFeNi high entropy alloy cluster growth and annealing on silicon: a classical molecular dynamics simulation study, Appl. Surf. Sci. 285 (2013) 810–816.
[52] S.I. Rao, C. Varvenne, C. Woodward, T.A. Parthasarathy, D. Miracle, O.N. Senkov, W.A. Curtin, Atomistic simulations of dislocations in a model BCC multicomponent concentrated solid solution alloy, Acta Mater. 125 (2017) 311–320.
[53] L.A. Greer, Metallic glasses, Science 267 (1995) 1947–1953.
[54] H.A. Davies, J. Aucote, J.B. Hull, Amorphous nickel produced by splat quenching, Nature 246 (1973) 13–14.
[55] C.J. Lin, F. Spaepen, Fe-B glasses formed by picosecond pulsed laser quenching, Appl. Phys. Lett. 41 (1982) 721–723.
[56] L. Zhong, J. Wang, H. Sheng, Z. Zhang, S.X. Mao, Formation of monatomic metallic glasses through ultrafast liquid quenching, Nature 512 (2014) 177.
[57] K. Zhang, S. Pan, W. Tang, Y. Zhang, B. Wei, Structural and bonding transformation of Al0.67CrCoCuFeNi high-entropy alloys during quenching, J. Alloy. Comp. 753 (2018) 636–641.
[58] M. Jafary-Zadeh, Z.H. Aitken, R. Tavakoli, Y.W. Zhang, On the controllability of phase formation in rapid solidification of high entropy alloys, J. Alloy. Comp. 748 (2018) 679–686.
[59] A. Mahata, M.A. Zaeem, Evolution of solidification defects in deformation of nano-polycrystalline aluminum, Comput. Mater. Sci. 163 (2019) 176–185.
[60] F. Otto, A. Dlouhý, C. Somsen, H. Bei, G. Eggeler, E.P. George, The influences of temperature and microstructure on the tensile properties of a CoCrFeMnNi high-entropy alloy, Acta Mater. 61 (2013) 5743–5755.
[61] A. Gali, E.P. George, Tensile properties of high-and medium-entropy alloys, Intermetallics 39 (2013) 74–78.
[62] A.J. Zaddach, C. Niu, C.C. Koch, D.L. Irving, Mechanical properties and stacking fault energies of NiFeCrCoMn high-entropy alloy, JOM 65 (2013) 1780–1789.
[63] B. Das, A.K. Nath, P.P. Bandyopadhyay, Online monitoring of laser remelting of plasma sprayed coatings to study the effect of cooling rate on residual stress and mechanical properties, Ceram. Int. 44 (2018) 7524–7534.
[64] N. Chobaut, D. Carron, S. Arsène, P. Schloth, J.M. Drezet, Quench induced residual stress prediction in heat treatable 7xxx aluminium alloy thick plates using Gleeble interrupted quench tests, J. Mater. Process. Technol. 222 (2015) 373–380.
[65] D. Srolovitz, T. Egami, V. Vitek, Radial distribution function and structural relaxation in amorphous solids, Phys. Rev. B 24 (1981) 6936.
[66] C.W. Tsai, Y.L. Chen, M.H. Tsai, J.W. Yeh, T.T. Shun, S.K. Chen, Deformation and annealing behaviors of high-entropy alloy Al0.5CoCrCuFeNi, J. Alloy, Composites 486 (2009) 427–435.
[67] L. Lilensten, J.P. Couzinié, J. Bourgon, L. Perrière, G. Dirras, F. Prima, I. Guillot, Design and tensile properties of a bcc Ti-rich high-entropy alloy with transformation-induced plasticity, Mater. Res. Lett. 5 (2017) 110–116.
[68] V.M. Miller, A.E. Johnson, C.J. Torbet, T.M. Pollock, Recrystallization and the development of abnormally large grains after small strain deformation in a polycrystalline nickel-based superalloy, Metall. Mater. Trans. A 47 (2016) 1566–1574.
[69] J. Li, Q. Fang, B. Liu, Y. Liu, C. Jiang, Twinning-governed plastic deformation in a thin film of body-centred cubic nanocrystalline ternary alloys at low temperature, J. Alloy. Comp. 727 (2017) 69–79.
[70] L. Zhao, K.C. Chan, S.H. Chen, S.D. Feng, D.X. Han, G. Wang, Tunable tensile ductility of metallic glasses with partially rejuvenated amorphous structures, Acta Mater. 169 (2019) 122–134.
[71] H. Bei, S. Xie, E.P. George, Softening caused by profuse shear banding in a bulk metallic glass, Phys. Rev. Lett. 96 (2006) 105503.
[72] A.J. Cao, Y.Q. Cheng, E. Ma, Structural processes that initiate shear localization in metallic glass, Acta Mater. 57 (2009) 5146–5155.